



Understanding Pre-Chamber Combustion Performance in a Closed-Cycle Model of a Novel Rotary Engine

Ioannis Nikiforakis, Gaurav Guleria, Mahmoud Koraïem, and Dimitris Assanis Stony Brook University

Curtis Collie, Tiago Costa, Piyush Kute, and Alec Shkolnik LiquidPiston, Inc.

Citation: Nikiforakis, I., Guleria, G., Koraïem, M., Assanis, D. et al., "Understanding Pre-Chamber Combustion Performance in a Closed-Cycle Model of a Novel Rotary Engine," SAE Technical Paper 2022-01-0396, 2022, doi:10.4271/2022-01-0396.

Received: 26 Jan 2022

Revised: 26 Jan 2022

Accepted: 19 Jan 2022

Abstract

A closed-cycle computational model of a non-Wankel rotary engine was thoroughly investigated to achieve optimal efficiencies, in a multitude of loading conditions relevant to automotive and aeronautical applications. Computational fluid dynamics (CFD) modeling was conducted in CONVERGE CFD, targeting the operation of a single pre-chamber and downstream main chamber engine system, roughly from 100 crank angle degrees (CAD) before top dead center (bTDC) to 100 CAD after top dead center (aTDC). In the developed framework, optimization studies involved main decision variables, including the engine's compression ratio (CR), the injector's position within the pre-chamber, the injector's nozzle hole count and nozzle hole diameters. Traditional and split-injection strategies for the introduction of diesel fuel

into the pre-chamber were evaluated by varying spray-related parameters including total injected mass, injection pressure, start of injection(s), and injection duration(s). The main metrics used to evaluate the engine's operation include (1) pre-chamber, main chamber, and overall combustion efficiencies and (2) closed-cycle average load performance determined by a relative indicated mean effective pressure metric. Additionally, the injected fuel phase state (liquid vs vaporized) and wall film thickness, if present, were used as performance metrics to determine fuel-air mixing success. Pre-chamber and main chamber maximum pressures were kept below 150 bar and injection pressures were limited at 1000 bar. As a result of this study, the best-performing cases demonstrated an overall combustion efficiency (η_c) that surpassed 90%, in both mid-load and high-load operating conditions.

Introduction

Ongoing climate change has led to the institutional establishment of stricter emission standards [1] that significantly impacted multiple technologies including internal combustion engines (ICEs), especially in the transportation sector. Notably, more than 20% of greenhouse gas emissions (GHGs) have been attributed to this sector [2], while emission pollutants such as NO_x , CO and particulate emissions due to unburned hydrocarbons (UHC) have monopolized the industry's concerns [3]. Consequently, the resulting push for increased fuel conversion efficiency has culminated in the implementation of novel technologies in ICEs, not only in terms of modus operandi, but also in core engine design. In respect to the former, research on conventional spark ignition (SI) and compression ignition (CI) modes of operation has been enriched, indicatively by homogeneous charge compression ignition (HCCI) [4], spark assisted HCCI [5] and reactivity controlled compression ignition (RCCI) [6]. Novelty in overall engine design can range from smaller modifications to the combustion chamber, such as the addition of an auxiliary pre-chamber [7, 8, 9] that can improve fuel

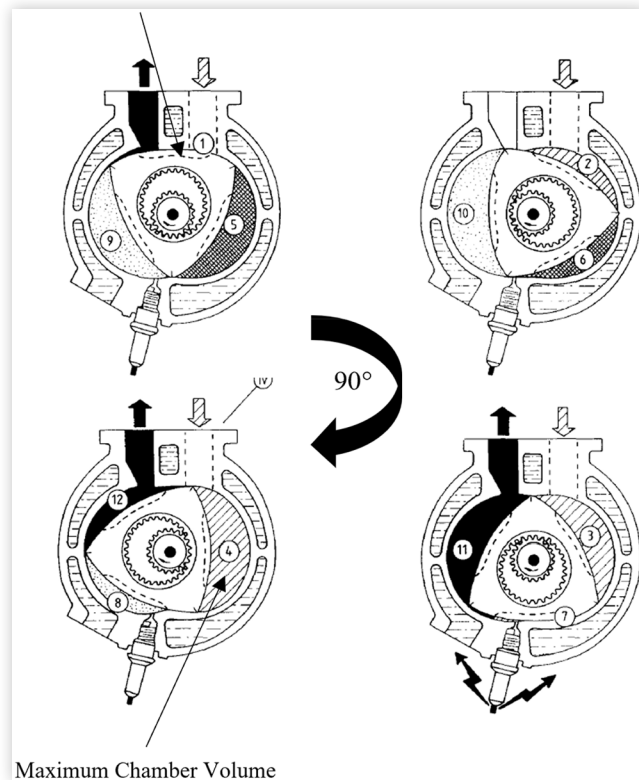
conversion efficiency. Larger modifications which include alternative piston, combustion chamber, and crankshaft reciprocating piston engine configurations [10, 11, 12] hold the potential to unlock even higher levels of fuel conversion efficiency. Finally, additional non-piston rotary architectures have been gaining increased attention.

Numerous rotary engine designs have been proposed in existing literature, with the most popular rotary apparatus consisting of the Wankel engine. A certain type of classification was implemented by Thompson et al. [13], where a multitude of designs has been divided into categories corresponding to their type of motion: vane, toothed-gear and oscillatory. The oscillatory category includes most of the identified designs by Thompson et al. [13], especially the ones patented earlier than most, in the majority of which a round rotor with multiple vanes rotated within a stator to form the engine's cam profile. While the most popular designs involve the patents of Britt [14] and Takahashi's [15] (SI) vane rotary engines, the toothed-gear type is the most uncommon among all suggested prototypes. The rotor and stator are concentrically geared together, with the design mechanism being more

popular in compressors and pumps. Lastly, the previously mentioned Wankel ICE, preliminarily assessed by Norbye [16], is considered the most prominent oscillatory-motion engine, with the design ultimately being commercialized [17]. In further detail, two rotors and a shaft are packaged in such a way that the space between the three rotor tips and the stator result to three separate gas volumes, with the engine operating under a four-stroke SI mode [13], as illustrated in Figure 1. Overall, the wide range of rotary engine patents culminated to certain sets of common features that evidently enabled the ability to rival or exceed the performance of conventional piston ICEs.

The extensive investigation of the multiple rotary engine designs [18, 19, 20] that have been proposed over recent decades can be mainly attributed to certain advantages over their conventional piston-crank ICE counterparts. Primarily, the theoretical power-to-weight ratio has been determined among the main drivers behind rotary engine technology [21], while the potential sealing difficulties [13] remain challenging for certain rotary engine designs. The specific drawback has been particularly present in CI regimes; thus, SI has been more prevalent in the assessed modes of combustion in rotary engine research [3]. Sealing issues can be successfully addressed using a low-blowby system design as shown by Nickerson et al. [22]. Furthermore, the reduced engine packaging requirements along with the increased performance

FIGURE 1 Illustration of Wankel engine operation through 90° of a single cycle, with all regions involved numbered from 1 through 12, as adapted from the work of Badr et al. [25]. Respective processes involve all induction, compression, combustion, expansion and exhaust, as manifested in the legend.



over various operating conditions [18] have rendered the technology increasingly attractive. In comparison to conventional piston ICEs, rotary engine designs feature increased mass-balancing [21] that has been enabled by significant weight reduction of semi-stationary parts and by integrating symmetrical engine design geometries. Additionally, the absence of valvetrain(s) should be highlighted since the particular fact leads to fewer vibrations while simultaneously decreasing overall system weight [23]. Increased compactness of the rotary engine design [24] has been in-part explained through the lower volume-to-power ratios, when compared to the most conventional ICEs in circulation, the Otto engines [23]. Further, researchers have argued for both increased volumetric [18] and fuel conversion efficiencies [20], over a wide range of operation, due to the gas exchange process being conducted in a more efficient manner [13].

Most of the previously stated advantages of rotary engine designs are agnostic to the operational combustion mode. Although most present-day rotary engines operate using SI combustion, the stated advantages are expected to mostly hold true for rotary engines that operate using the CI combustion regime. Limited prior research has been identified for rotary engines under CI modi operandi and thus should be further investigated to understand if a higher fuel conversion efficiency can be unlocked in comparison to SI combustion. A review conducted by the Army Research Lab indicates that “significant opportunities in all respects exist to improve efficiency, performance, and durability of the rotary engines by using today’s advanced technologies” [26]. Specifically, Louthan [27] altered a single-rotor Wankel engine to operate on heavy fuels, which would be suitable for unmanned air vehicles (UAVs). Louthan investigated the installation of a high-pressure fuel injection system through which the engine would operate under the proposed conditional compression ignition (CCI) regime. Furthermore, Shapovalov [23] implemented a different engine apparatus, which nevertheless operated on oscillatory motion, just as Louthan’s design. The proposed Vladimir Shapovalov (VS) engine was again considered for auxiliary power units (APUs) and would probably be further examined in aerospace power system applications. In summary, there is an opportunity to further investigate CI combustion mode performance and specifically explore the additional positioning of pre-chambers in oscillatory motion engines for mixing-controlled regimes. As a result, this body of work will detail the feasibility study of a LiquidPiston Inc. (LPI) prototype engine that has been computationally modeled to investigate the performance of an actively fueled pre-chamber combustion system in a novel rotary engine, operating on conventional light diesel fuel under CI mode conditions.

Computational Methodology

The proposed computational fluid dynamics (CFD) model was implemented in conjunction with LPI proprietary engine research and development efforts to explore prototype

combustion chamber geometries digitally and at a significantly reduced cost in comparison to manufacturing prototype variants. Since the CFD model is at the core of the computer-aided engineering effort, the evaluated geometry cannot therefore be fully validated, due to the non-existence of the physical engine prototype. Necessary boundary conditions were determined in-house by LPI from validated 1-D engine simulations or other 3-D iterative open-cycle simulations using industry standard practices.

Computational Tools and Facility

The computational facility used to resolve the model design points is Stony Brook University's SeaWulf computational cluster at the Institute for Advanced Computational Science (IACS). SeaWulf is powered by 164 computational nodes, each boasting 128 GB of RAM and 14 cores for a total computational power of 240 teraflops.

The numerical CFD model was created using CONVERGE Studio and solved using CONVERGE CFD 3.0 (versions 3.0.14 - 3.0.20) [28]. For postprocessing, MATLAB 2021a was used for calculation of flow-field variables and plot generation, while Tecplot 360 2020 R2 was used for 3-D visualizations and generation of contour plots.

Base Computational Model

Computational Domain The engine's computational domain consists of two regions: a combustion chamber and a pre-chamber mounted on top of it. The regions are enclosed between an eccentric rotor, and a semi-spherical shell. In addition, the pre-chamber has a side-mounted fuel injector, spraying fuel perpendicular to the mounting direction.

One of the benefits of the novel rotary engine can be seen when investigating the combustion chamber's volume sweep, with respect to crank angle degrees (CAD), against that of a traditional reciprocating piston engine. Comparing the novel rotary engine with a traditional one of a similar volume, compression ratio (CR), and engine speed, the rotary swept profile is more rounded at top dead center (TDC) compared to a traditional engine, as manifested in Figure 2. The flattening of the curve near TDC makes the engine remain at a near-constant clearance volume over a longer span of CAD than a traditional reciprocating engine.

Physical Models and Solution Time Turbulence was numerically modeled using Reynolds-averaged Navier-Stokes (RANS) re-normalization group (RNG) k- ϵ with a standard wall function [29]. The fuel spray was computationally modeled using the modified Kelvin-Helmholtz, Rayleigh-Taylor models for breakup and the no-time-counter (NTC) method for collisions [30]. As for turbulent dispersion, the O'Rourke model was used, along with the Frossling correlation for droplet vaporization [31]. In addition, interaction with chamber walls was modeled using O'Rourke's wall film model [32]. The combustion event was modeled using the SAGE detailed chemistry solver with adaptive zoning [33]. To reduce

FIGURE 2 Normalized volume sweep comparison of the novel rotary engine to an equivalent traditional reciprocating piston engine.

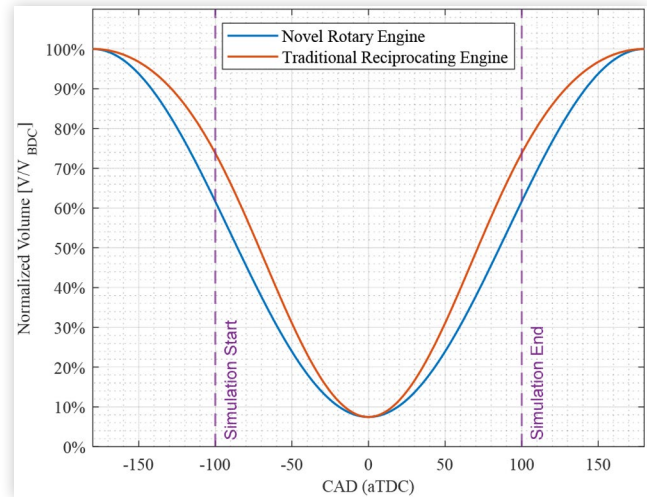
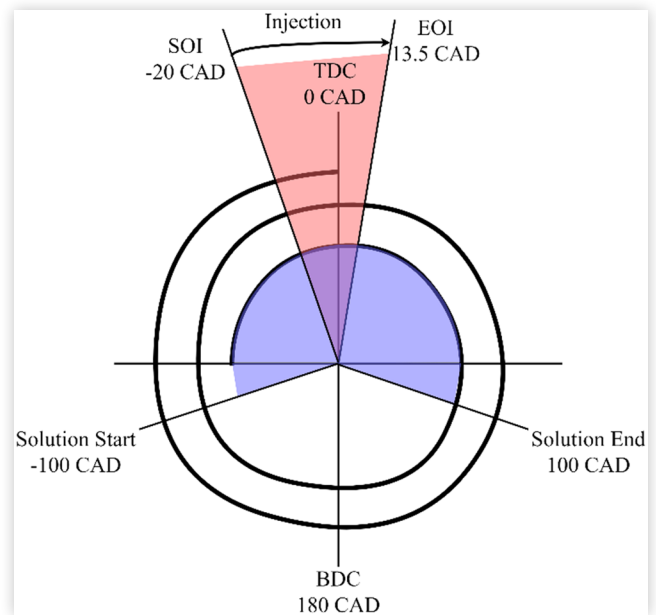


FIGURE 3 Base model's timing diagram, showing SOI at 20 CAD (bTDC) for a duration of 33.5 CAD.



computational time, the combustion regions (pre-chamber and main chamber) are activated at 50 CAD before top dead center (bTDC). The physical models work in tandem with a 43-species, 168-reactions chemical kinetic mechanism for diesel combustion, as well as a data file containing thermodynamic properties for 621 species [34].

The model was solved in a closed cycle from 100 CAD (bTDC) to 100 CAD after top dead center (aTDC), covering the compression, ignition, and expansion processes inside the main chamber and its pre-chamber. The model's spray had a base start of injection (SOI) at 20 CAD (bTDC), and an injection duration of 33.5 CAD, as shown in the timing diagram of Figure 3. The spray design elements were later varied parametrically to investigate different operating conditions.

Initial and Boundary Conditions The model's boundary conditions were determined using a 1-D GT-POWER model, built by LPI, and correlated with relevant experimental data, where available. Initial temperature, pressure and species were based on iterative open-cycle analysis using CONVERGE CFD, also performed in-house by LPI using their proprietary models. The results from the open-cycle model, were mapped to initialize the closed-cycle model that is considered in this study. For the initial design point, the combustion chamber and the pre-chamber were initialized with a mixture of mainly air and exhaust gas residue (from the open-cycle data), with an initial pressure of 3.9 bar. A summary of the boundary conditions at the wetted surfaces for the closed-cycle model is shared in [Table 1](#).

Computational Grid The novel rotary engine model utilized CONVERGE's cut-cell adaptive meshing. Model's grid convergence was tested with a base grid size varying from 2.8 mm through 1.6 mm. Additional embedding settings involved sequential embedding which covered the injector spray targeted zone during injection with a scale of 4, permanent regional embedding of a scale of 1 that applied to the combustion chamber, and permanent embedding with a scale of 3 or 4 (for the 2.8 mm grid) set at combustion chamber boundaries. Moreover, the model used adaptive mesh refinement (AMR), with velocity and temperature gradient activation (1.0 m/s and 2.5 K respectively) at a refinement scale of 3. To continue, a y^+ activated AMR with a refinement scale of 4, and a target y^+ of 30 were implemented. In further detail, [Figure 4](#) illustrates an x-y

TABLE 1 Boundary conditions of wetted surfaces for the closed-cycle engine model.

Boundary	Region	Temperature	Boundary Motion
Rotor Surface	Main Chamber	450 K	Moving
Pre-chamber	Pre-chamber	773 K	Stationary
Chamber	Main Chamber	523 K	Stationary
Apex Seals	Main Chamber	400 K	Stationary

FIGURE 4 Model grid cross section at 90 CAD (aTDC) overlaid across rotary engine geometry's z-axis.

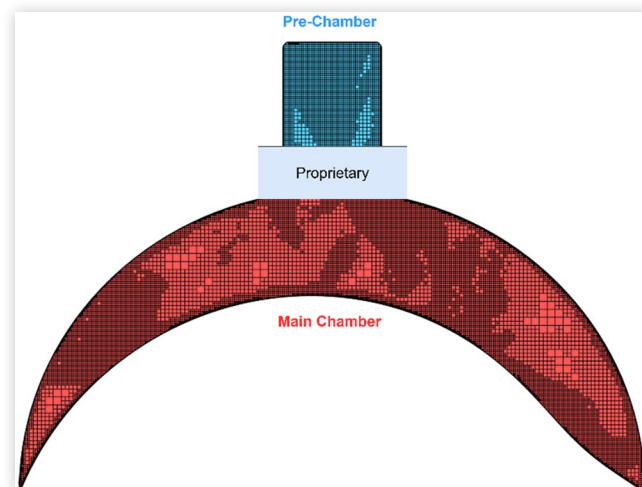
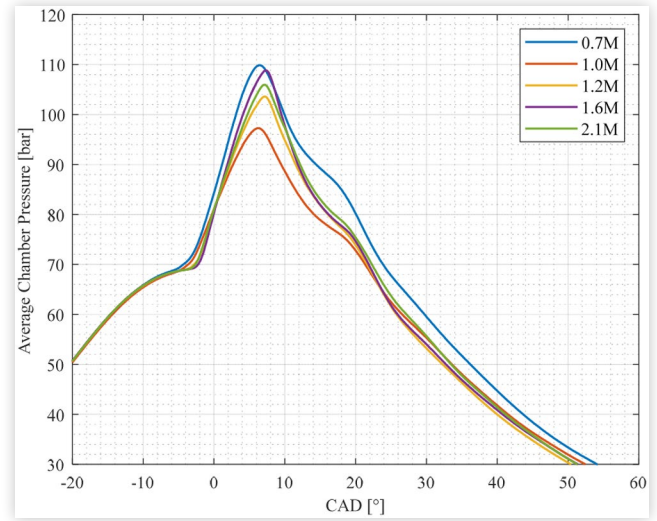


FIGURE 5 Pressure trace showing grid convergence for different base grid sizes as well as different embeddings.



plane cross section of the model's computational mesh, while the aforementioned grid convergence study was conducted by testing different grid configurations ([Figure 5](#)). From a maximum number of 0.7 million (M) cells to 2.0M cells, convergence was observed at a maximum cell number of 1.2M cells, with a maximum error of 3% for a 5 CAD window centered around peak pressure, and an error of 1% or less for all remaining solution time. Manifestly, [Figure 5](#) depicts the variation in pressure trace with the grid configuration sweep.

Simulations

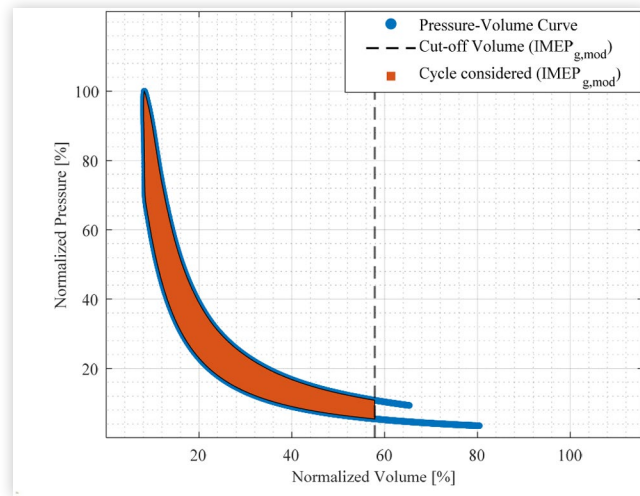
Our implemented design of experiments (DOE) involved progressive variations of several decision variables, carried out in a multi-step analysis. Multiple simulations were concurrently performed to evaluate one primary independent variable at a time. Multiple sets of simulations, evaluating multiple variations of independent variables could then be used in tandem to determine the next optimal baseline condition to iterate from. This allowed us the ability to cover a wide range of input variations in a trend wise manner before combining all beneficial behaviors to realize the full performance benefits. The varied input parameters were mostly focused on iterative geometry and fuel spray configurations. Performance benefits were measured using primarily the following volume-normalized, modified gross indicated mean effective pressure metric:

$$\text{IMEP}_{\text{g,mod}} = \frac{\oint p dV}{4 \times 10^{-5} \text{ m}^3} \quad (1)$$

where, $\text{IMEP}_{\text{g,mod}}$ is the gross indicated mean effective pressure criterion, p is the in-cylinder pressure and V is the cylinder volume.

Further detailing involved engine performance on two core metrics identified in combustion efficiency (η_c) and indicated mean effective pressure (IMEP), with the latter proving

FIGURE 6 Representation of cut-off volume and pressure-volume curves being considered in the established $IMEP_{g,mod}$.



to be particularly challenging. Specifically, the difficulty in quantifying gross IMEP ($IMEP_g$) appertained to the unavailability of open-cycle simulations, where the complete engine work could be assessed. Instead, the engine was examined in closed-cycle conditions, roughly from 100 CAD (bTDC) to 100 CAD (aTDC). As a result, a cut-off volume was determined at 0.04 L and would replace the displaced volume in the conventional IMEP's denominator, with the criterion being established as $IMEP_{g,mod}$. Consequently, the engine's work would be measured in all compression, combustion and expansion phases being involved below the particular point in the pressure-volume curve, as illustrated in Figure 6. In that, volume and pressure were normalized to volume at bottom dead center (BDC) and peak pressure (p_{peak}), respectively. The described definition of the specific performance metric was expressed through Equation (1). Moreover, η_c was investigated in both pre-chamber and main chamber, with the overall metric accounting for heat release in both engine compartments. Lastly, engine operation was limited, since fuel injection pressure and peak cylinder pressure, in both chamber and pre-chamber, would be kept under 1000 and 150 bar, respectively.

In relation to the model's input, conditioned iterative sensitivity analyses were performed. Rather than design optimization, the decision variables in play were altered to allow for informed decisions between the various steps of the DOE. In that, geometric features of chamber and pre-chamber, injector structure and positioning, as well as injection timings were deemed variable. Notably, several quantities of injected mass were input in the aggregate simulations, to assess both mid-load and high-load ranges.

Engine Geometry The engine geometry involved the integration of three separate main chambers and three respective pre-chambers that accommodated all fuel injections. With simulations focusing on one of the particular assemblies, as illustrated in Figure 4, the design was altered mainly in terms of compression ratio, in which the volume of the pre-chamber was modified. That being said, the particular compression

ratios which were tried and tested have been rigorously analyzed in the *Results & Discussion* section.

Injector Geometry Geometrical features of the injector predominantly included nozzle hole count and hole diameter. Variations in the former were followed by sensitivity analyses of the latter, in each step of the process, in order to thoroughly assess their impact on the selected η_c and $IMEP_{g,mod}$ metrics. Notably, the specific features were morphed in such a way to additionally account for the limitations being imposed, in terms of injection pressure and p_{peak} , in both main chamber and pre-chamber.

Injection Timing The timing of injection(s) was paramount in the conducted assessment studies. SOI sweeps were iteratively implemented, ranging approximately from -20 to 5 CAD (aTDC), in single-injection cases. Additionally, in simulations accommodating multiple injections, with a wide range of splits being investigated in the *Results & Discussion* section, numerous injection strategies were evaluated. Consequently, injection duration was naturally examined, with the particular parameter being varied accordingly, at each step of the way.

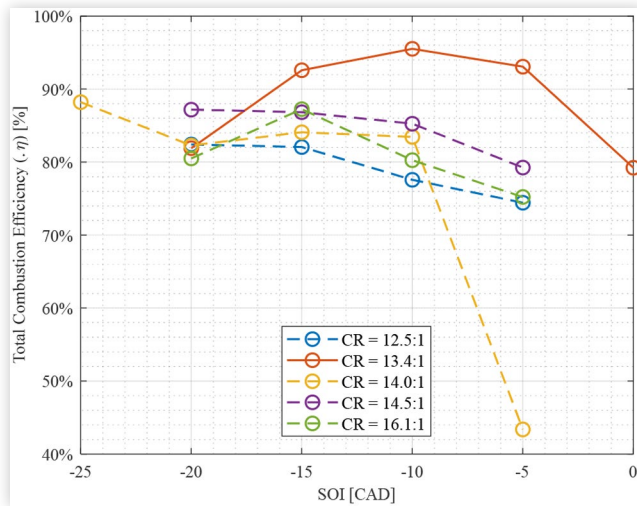
Results & Discussion

Over 200 closed-cycle CFD simulations were performed as part of this feasibility study for the LPI prototype rotary engine. The variations were progressively applied throughout multiple stages, with the emerging results providing valuable information on engine operation. Primarily, given that the analysis should fundamentally assess two separate loading conditions, two respective sets of injected fuel mass ranges were assessed. The lower one involved 5 to 7 mg of diesel, while the one corresponding to higher loads accommodated 8 to 10 mg of the same fuel. Naturally, existing in-cylinder mixture prior to fuel injections additionally impacted loading conditions, with the respective air-to-fuel ratio (AFR) and thus equivalence ratio (ϕ) being further investigated. Overall, all essential variations were analyzed in the current section, followed by extensive reporting on the emerging simulation results, while they in turn were rigorously discussed. The results being enlisted in this section's tables and depicted in the section's figures summarize these simulated cases.

Mid-Load Operation

The pre-chamber volume was adjusted to conduct a parametric study comparing different CRs, sweeping through 12.5:1, 13.4:1 (base CR), 14.0:1, 14.5:1, and 16.1:1 under mid-load conditions at 6000 rpm. The cases had an initial chamber pressure of 3.9 bar, injecting 6.0 mg of fuel through a 4-nozzle spray with 85 μ m diameter (nozzle hole), keeping the maximum injection pressure at 1012 bar. A fuel injection sweep was performed for each CR to compare resulting combustion efficiencies. Figure 7 shows the total combustion efficiency plot against SOI timing for different CRs. The figure

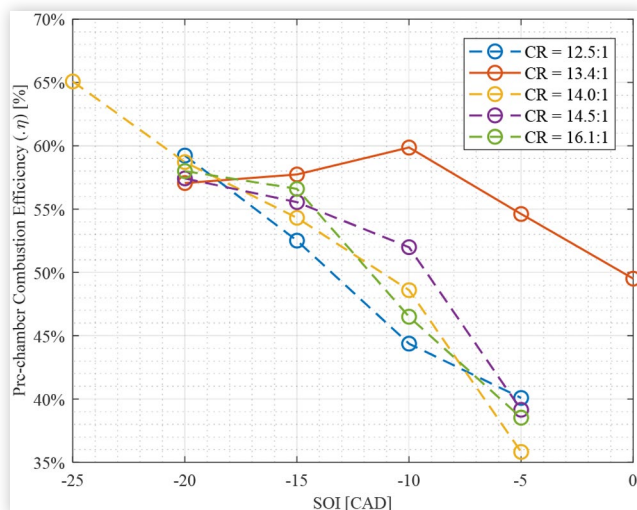
FIGURE 7 Comparison of total combustion efficiency at different SOI timings, for different compression ratios.



illustrates that the base CR of 13.4:1 had the highest overall combustion efficiency along its sweep of SOI timings, with optimal values being observed between 15 to 5 CAD (bTDC), followed by 14.0:1 and 14.5:1.

At lower and higher CRs than 13.4, a decrease in combustion efficiency was noted. This is due to the altered pre-chamber size to change the CR while maintaining the same engine geometry. The reduced pre-chamber volume and surface area impacted the ability of the prechamber's hot surface to properly vaporize and burn fuel efficiently. The combined effect of reduced pre-chamber performance in addition to the change in CR caused a limitation on the range of useable CRs for the current engine configuration and pre-chamber design. This effect can be seen in Figure 8, which depicts the pre-chamber combustion efficiency sweep. Note the very low pre-chamber combustion efficiency when the CR

FIGURE 8 Comparison of pre-chamber combustion efficiency at different SOI timings, for different compression ratios.



is 14:1, which is the main factor for the lower total combustion efficiency.

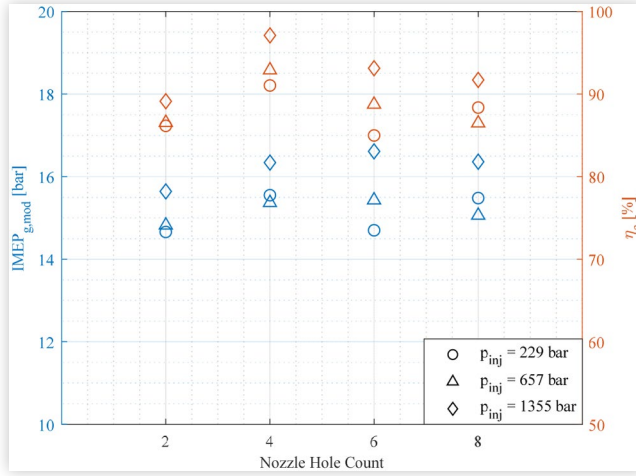
Following the engine's CR assessment, the engine's scavenging was additionally examined in the existing in-cylinder mixture concentrations, prior to fuel injections. The trapped air mass that was present at the cylinder in the beginning of closed-cycle simulations, at approximately 100 CAD (bTDC), exerted a significant effect on simulated results, for multiple loading conditions. At the lower end of the latter spectrum, injected mass of 6 mg of fuel under different scavenging regimes resulted in significantly different engine performance. Essentially, variation in scavenging was input in the established modeling schemes by the initialization of different conditions, in which initial pressure in both chamber and pre-chamber was the most decisive. Indicatively, higher initial pressure in the region allowed for greater trapped air mass, which in turn resulted in greater scavenging. As illustrated in Table 2, for SOI fixed at 10 CAD (bTDC), there was clear evidence of higher performance with increased scavenging, in terms of both η_c and $IMEP_{g,mod}$, with the gains in the former being clear-cut in the pre-chamber. Manifestly, an increase in initial pressure at both regions, in the order of 20%, allowed for increased trapped mass (air), translating to greater combustion efficiency. Seemingly, greater trapped mass culminated to greater gains in effective pressure.

Nozzle hole count undoubtedly impacted the rotary engine's performance. Considering the three injection pressures that were primarily examined, nozzle hole count was altered accordingly to achieve the desired pressure threshold. With the injection duration being fixed among all investigated configurations and the injected fuel mass being constant at 6 mg, nozzle hole diameter was additionally modified in an attempt to exert increased control to peak injection pressure. Throughout the examined cases, the selection of 4 nozzle holes seemingly performed better overall, as depicted in Figure 9. In that, both $IMEP_{g,mod}$ and η_c at the highest injected pressure outperformed their counterparts at 2, 6 and 8 nozzle holes overall. Naturally, both metrics were identified higher at greater injection pressure, with maximum η_c being achieved where the reported pressure at the main chamber peaked, at approximately 122 bar. When transitioning from injection sprays of 2 to 4 nozzle holes, the diameter was reduced in order to ascertain the same injection pressure. By doing so, smaller particles were formed, which resulted in enhanced vaporization, with the surface-to-volume ratio being naturally higher,

TABLE 2 Indicated performance metrics of the simulated engine model, for two different types of scavenging.

Property	Initial Scavenging	Final Scavenging
Pre-chamber p_{peak}	74.28 bar	85.58 bar
Location (Pre-chamber)	9.90 CAD (aTDC)	7.70 CAD (aTDC)
Main Chamber p_{peak}	64.52 bar	78.17 bar
Location (Main Chamber)	15.10 CAD (aTDC)	13.20 CAD (aTDC)
HRR_{peak}	10.34 J/CAD	8.37 J/CAD
Location	6.70 CAD (aTDC)	3.41 CAD (aTDC)
Pre-chamber η_c	49.60%	59.86%
Total η_c	85.50%	95.52%
$IMEP_{g,mod}$	13.78 bar	14.75 bar

FIGURE 9 IMEP_{g,mod} and η_c scatters against nozzle hole count for the three different peak injection pressures (legend). In terms of the performance metrics, the former corresponds to the left y axis and the latter accounts for the right one.



as evident in Figure 10 for the earlier combustion cases. Consequently, temperature conditions allowed for higher fuel amounts being entrained in the premixed phase. On the other hand, the cases associated with injection sprays featuring 6 and 8 nozzle holes performed worse on average than the case of 4 nozzle holes, in terms of both combustion efficiency as well as modified gross indicated mean effective pressure. Seemingly, fuel vaporized at a faster rate, which did not allow for a long enough period during combustion to effectively transition to the diffusion-burn phase. The resulting heat release was greater overall in the case of 4 nozzle holes which also led to a higher level of combustion efficiency. Despite peak pressures being reported marginally higher, with heat transfer loss rates being in turn increased, the overall impact of the relatively increased heat release benefited performance.

FIGURE 10 IMEP_{g,mod} and η_c scatters against SOI for the two different nozzle hole diameters (legend). In terms of the performance metrics, the former corresponds to the left y axis and the latter accounts for the right one.

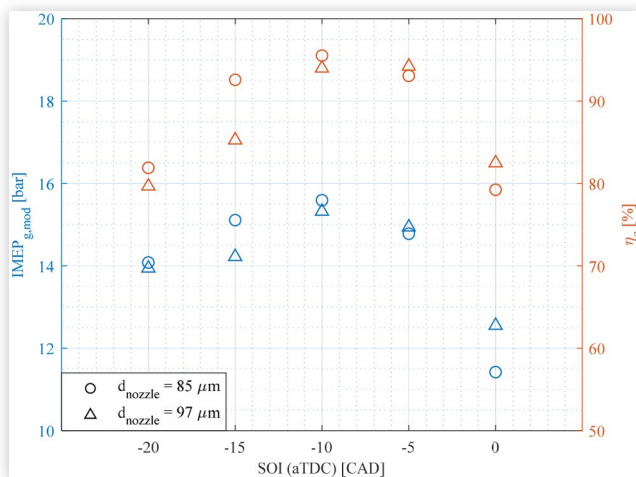
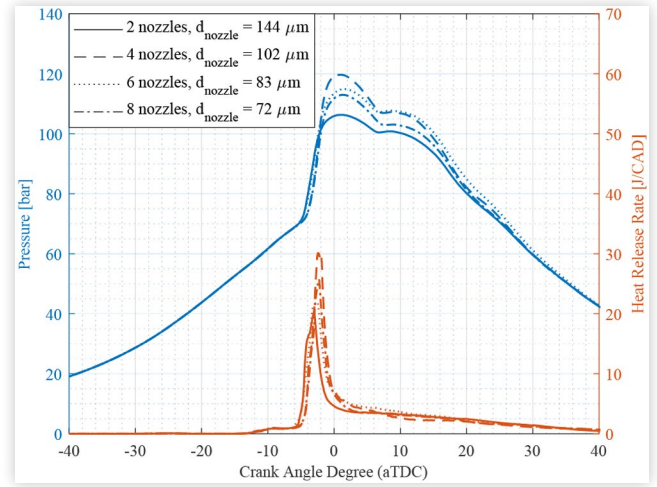


FIGURE 11 Pressure trace and heat release rate plotted against CAD for all 2, 4, 6 and 8 nozzles, when injection pressure was kept at 657 bar.



Therefore, the particular sweet-spot configuration was achieved in the case of 4 nozzle holes.

As depicted in Figure 11, the injector with 4 nozzles provided the greatest overall heat release rate over this closed-cycle comparative evaluation. It is also evident that, relatively early combustion plays a decisive role in terms of increasing effective pressure gains, which allows for higher average pressures to be achieved during the expansion stroke. Thus, combustion phasing was identified as having a critical role in leading to higher IMEP_{g,mod} values. Furthermore, increased injection pressure again led to advanced combustion, resulting in higher peak pressures, which in turn culminated to additional work extraction from the expansion process, in comparison with the cases of lower injection pressure. The latter was evident in Figure 9, since increase in injection pressure, especially from 657 bar to 1355 bar, resulted in greater values of IMEP_{g,mod} overall. Manifestly, gains in the amount of heat release significantly benefited overall combustion, despite increased rates of heat transfer being achieved due to higher peak pressures and temperatures. While the latter conditions yielded shorter ignition delays, elevated expansion work benefited the overall configuration, in spite of the increased heat transfer losses. Notably, the pressure injection limit was set at 1000 bar after these preliminary runs and was conserved throughout the rest of this feasibility study.

In terms of nozzle hole diameter, alterations in the specific parameter were followed by changes in injection duration, while nozzle hole count was kept constant. In such a manner, we could better isolate the impact of nozzle hole diameter on engine performance, with injection duration nevertheless being in turn altered to limit peak injection pressure. Indicatively, Figure 10 depicts the two main performance metrics results, when SOI was initiated at all -20, -15, -10, -5 and 0 CAD (aTDC), for two different nozzle hole diameters being implemented (85 and 97 μm). Evidently, the lower nozzle hole diameter case outperformed the greater one, when SOI was advanced from 20 to 10 CAD (bTDC). Apparently, advances in SOI culminated to the higher-diameter case

performing better than its lower counterpart, but at a lower overall level if compared to the cases of earlier SOI. Consequently, the lower nozzle hole diameter (85 μm) should be selected, particularly if SOI is phased earlier than -10 CAD (aTDC), since greater peak pressures would lead to higher work extraction from gas expansion, benefiting the overall design [35].

Figure 10 additionally provides valuable information on SOI impacting performance. Manifestly, overall engine performance was optimized when SOI occurred at -10 CAD (aTDC) for the particular case. Naturally, earlier combustion phasing in the lower SOI spectrum resulted to a significant portion of the combustion process happening during compression, resulting in lower overall work extraction. Later combustion phasing, past -10 CAD (aTDC), resulted in significantly decreasing heat transfer due to the notable reduction in peak pressures and temperatures, and shifted operation to the region of diminishing returns. Manifestly, the choice where performance was optimized comprised of the sweet spot between the two aforementioned trends that evidently affected engine performance.

Notably, alteration of external conditions would again influence the assessed system's performance, and at a critical degree. Were the particular engine to be implemented in APUs of aviation systems, as cited in the respective literature for technologies incorporating rotary mechanisms [23], parameters such as temperature and pressure should be altered in the investigated model. Consequently, that would affect initial species concentrations in both pre-chamber and main chamber, as well as initial temperature and pressure in the particular regions when considering model initialization. In that, one of the greatest alterations was identified in initial pressure, in both chamber and pre-chamber regions, where the latter roughly increased by 18%, when compared to the lower-diameter case illustrated in Figure 10. Additionally, optimal performance was achieved when the nozzle hole diameter was increased from the assessed 85 μm of the previous configuration to 125 μm , while nozzle hole count was maintained (four). In further detail, injected fuel mass again amounted at 6 mg, while SOI was identified at 20 CAD (bTDC). Overall, performance in the specific case was expressed through series of metrics, as listed in Table 3.

TABLE 3 Performance metrics of the best-performing case in the mid-load region.

Property	Optimal Case @ Mid-Load
Pre-chamber p_{peak}	142.98 bar
Location (Pre-chamber)	7.11 CAD (aTDC)
Main Chamber p_{peak}	147.60 bar
Location (Main Chamber)	2.61 CAD (aTDC)
HRR_{peak}	22.84 J/CAD
Location	-6.29 CAD (aTDC)
Pre-chamber η_c	81.27%
Total η_c	98.00%
$\text{IMEP}_{\text{g,mod}}$	17.62 bar

High-Load Operation

The performance of the model was also investigated at high-load conditions. In order to achieve that, the mass of the injected fuel was increased from 6 mg in the mid-load cases, up to 10 mg. For this study the initial SOI timing was 5 CAD (bTDC) and the injection duration was kept at 30 CAD. The injector comprised of 4 nozzle holes which diameter was set at 125 μm , while peak injection pressure was kept at 1000 bar. Pressure and heat release rate plots in the pre-chamber and the main chamber for the closed-cycle run of this case are shown in Figure 12. The important combustion metrics relevant to the performance of the engine can be viewed in Table 4.

As evident in Table 4, increasing the mass of injected fuel resulted in lower combustion efficiency when compared to the mid-load cases. Wall film in the pre-chamber is manifested in Figure 16, and detailed fuel stratification is additionally evident in Figure 13 during combustion, at both front view (upper row) and side view (lower row). Naturally, a 60% increase in fuel injection should reduce combustion efficiency, while accumulation of increased film on pre-chamber walls

FIGURE 12 Pressure and heat release rate plot in pre-chamber and main chamber for the single-injection high-load case.

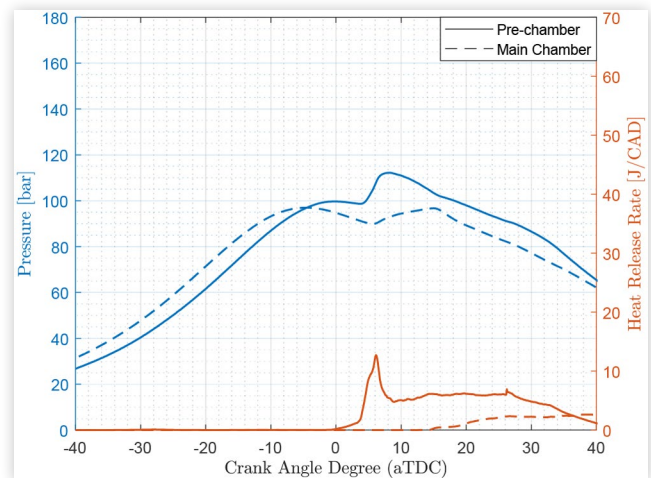
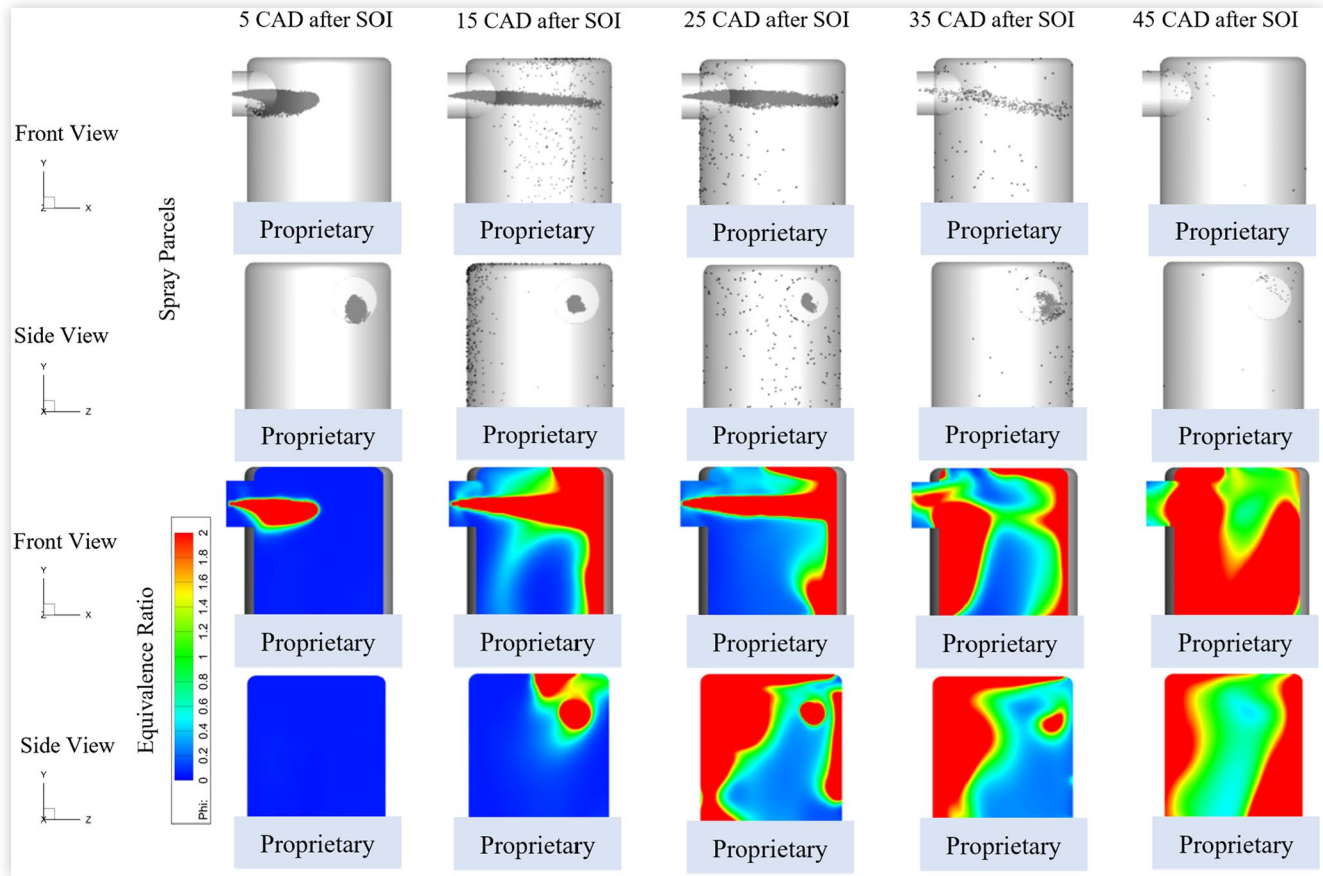


TABLE 4 Injected fuel and indicated performance metrics of the simulated engine model for the single-injection high-load case

Property	High-load (Single Injection)
Fuel Mass	10 mg
Pre-chamber p_{peak}	112.21 bar
Location (Pre-chamber)	8.23 CAD (aTDC)
Main Chamber p_{peak}	96.97 bar
Location (Main Chamber)	-4.66 CAD (aTDC)
HRR_{peak}	12.71 J/CAD
Location	6.14 CAD (aTDC)
Pre-chamber η_c	44.63%
Total η_c	80.75%
$\text{IMEP}_{\text{g,mod}}$	22.75 bar

FIGURE 13 3D visualizations (pre-chamber) of spray parcels and equivalence ratio, in two engine views, front (top) and side (bottom) for single injection.



would deter overall performance. Nevertheless, the $IMEP_{g,mod}$ achieved for this case was 22.75 bar and was significantly greater than the 17.62 bar reported in the best case of the mid-load runs. The particular performance can be attributed to fuel being increased by more than 60%, while air was raised by 30%.

Figure 13 illustrates the spray parcels and ϕ distribution for the front and side views of the pre-chamber while Figure 14 shows the temperature and OH mass fraction for the same regions. Figure 15 and Figure 16 depict the variation of fuel mass and state for this case throughout the investigated closed cycle. The plots track the fuel injected in the pre-chamber and the main chamber and illustrate the states of the injected fuel as the simulation progresses. The vaporized fuel was a key metric, and the DOE was setup to maximize fuel vaporization in the pre-chamber, in order to optimize performance in terms of combustion efficiency. Figure 15 further manifests that there was no fuel in the main chamber, in the liquid state or as the wall film, at any point within the closed-cycle simulation.

Figure 16 depicts that a significant amount of fuel was in the liquid state as it was injected in the pre-chamber when injection commenced. However, as the simulation progressed, fuel almost completely vaporized at about 30 to 35 CAD (aTDC). Further, the aforementioned increments in air mass were enabled through increased regional pressure initialization at both pre-chamber and main chamber. Given that

trapped air mass for this case was increased at a significantly lower rate than injected fuel, when compared to all exhibited mid-load cases, overall AFR dropped by even 30% in relation to the optimal mid-load case. Overall, the combination of the accumulated fuel on the walls of the pre-chamber during combustion and lower AFR resulted in lower combustion efficiency than in the mid-load cases.

In an effort to increase vaporization rates of the liquid film from the pre-chamber walls during core combustion, a split-injection strategy was investigated. The injection event was divided into the pilot injection and main injection, where 1 mg of the fuel was injected during the former and 8 mg of fuel were injected during the latter. The injection duration was 3 CAD for the pilot injection and 24 CAD for the main injection. Injection durations for both injections were specified so that injection pressure was kept at 1000 bar. The injector setup was also changed to achieve better combustion efficiency and $IMEP_{g,mod}$. In detail, the nozzle diameter was reduced from 125 μm to 85 μm and the number of injector nozzles was increased from 4 to 8. This was done in an attempt to decrease the fuel droplet size and to enhance vaporization of the fuel in the pre-chamber. For the current case study, SOI was 30 CAD (bTDC) for the pilot injection and 10 CAD (bTDC) for the main injection. Additionally, the total mass of injected fuel was reduced to 9 mg, in order to achieve higher combustion efficiency. Moreover, pressure and heat release rate plots in pre-chamber and main chamber, for the

FIGURE 14 3D visualizations (pre-chamber) of temperature and OH mass fraction, in two engine views, front (top) and side (bottom) for single injection.

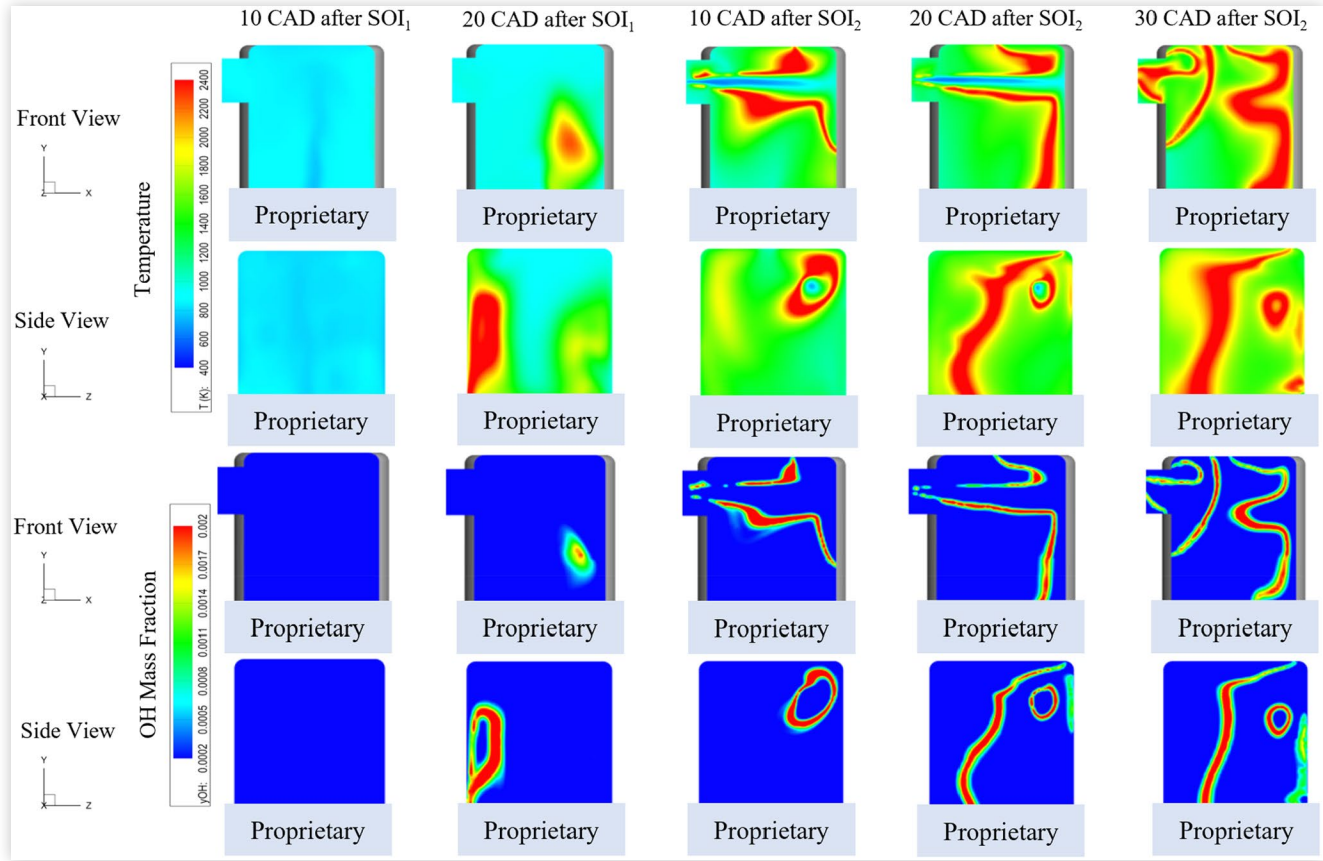


FIGURE 15 Fuel mass and state in the main chamber for the single-injection high-load case.

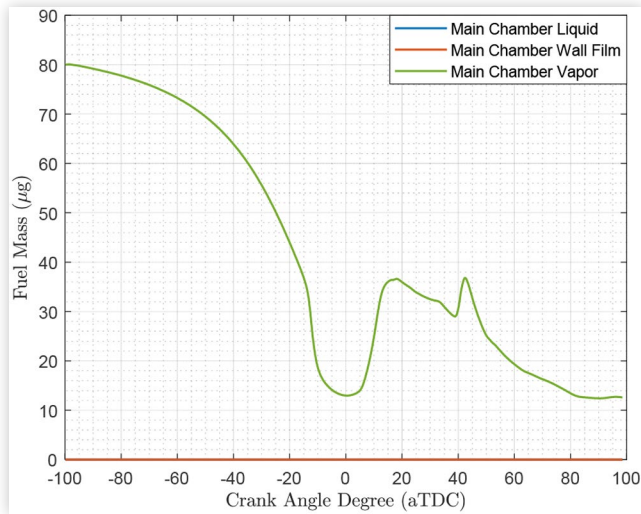
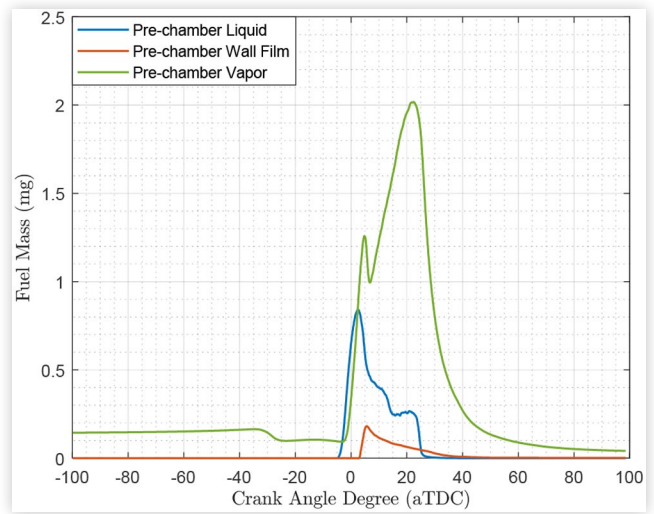


FIGURE 16 Fuel mass and state in the pre-chamber for the single-injection high-load case.



closed-cycle run, are illustrated in Figure 17. Important combustion metrics, relevant to engine performance were listed in Table 5.

Evidently, the split-injection case produced higher load with less fuel, associating the particular strategy with significantly higher levels of performance than the single-injection

high-load case. Peak pressures for this case were measured 141.20 bar for the pre-chamber and 133.2 bar for the main chamber, and were significantly higher than in the single-injection high-load case which was earlier discussed (Table 4). Seemingly, the $IMEP_{g,mod}$ for the double injection case was 23.88 bar, which is about 5% higher than the single injection

FIGURE 17 Pressure and heat release rate plot in pre-chamber and main chamber for the split-injection high-load case

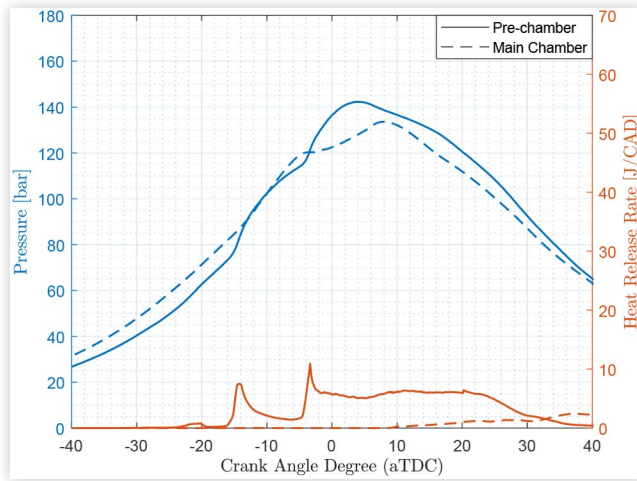


TABLE 5 Injected fuel and indicated performance metrics of the simulated engine model for the split-injection high-load case and their relative change in comparison to the single-injection high-load case.

Property	Split Injection	Δ from Single Injection
Fuel mass	9 mg	- 10%
Pre-chamber p_{peak}	141.20 bar	+ 25.84%
Location (Pre-chamber)	4.00 CAD (aTDC)	- 4.23 CAD
Main Chamber p_{peak}	133.20 bar	+ 37.36%
Location (Main chamber)	7.70 CAD (aTDC)	+ 12.36 CAD
HRR _{peak}	11.20 J/CAD	- 11.88%
Location	-3.40 CAD (aTDC)	- 9.54 CAD
Pre-chamber η_c	59.70%	+ 33.77%
Total η_c	86.18%	+ 6.72%
IMEP _{g,mod}	23.88 bar	+ 4.97%

case, even though injected fuel mass was reduced by approximately 10%. Earlier peak pressures when injection was split (Table 5) were reportedly higher by more than 25% in the split-injection case. Seemingly, elevated work extraction was achieved from the expansion process, resulting in the recorded increments in terms of effective pressure. Nevertheless, the disparities between the two cases in terms of combustion efficiency were far greater than IMEP_{g,mod} and p_{peak} . In fact, higher temperatures were recorded in the pre-chamber prior to the main injection. Consequently, fuel vaporization was conducted at higher rates, as again evident in the density of spray parcels on the pre-chamber walls, as shown when comparing Figure 13 with Figure 20. The pilot injection in the split-injection case resulted in earlier combustion within the closed cycle, in comparison to single injection, as depicted between Figure 14 and Figure 21, where OH mass fractions are illustrated.

Figure 18 depicts the fuel mass and state in the main chamber for the split-injection case, in which no wall film or liquid fuel were observed. Enhanced vaporization in the

FIGURE 18 Fuel mass and state in the main chamber for the split-injection high-load case.

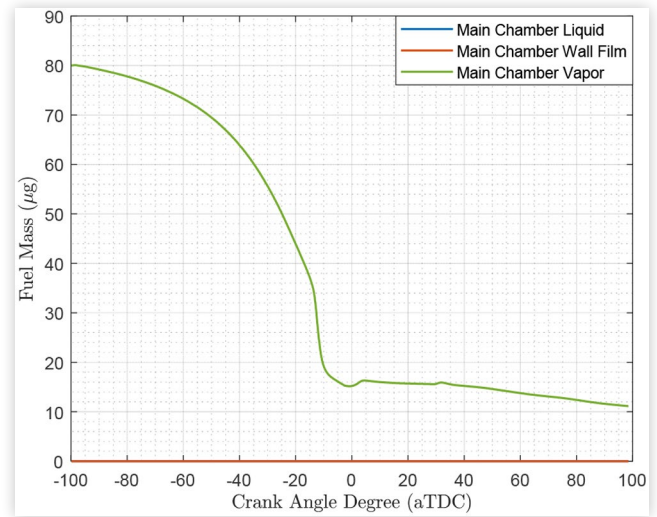
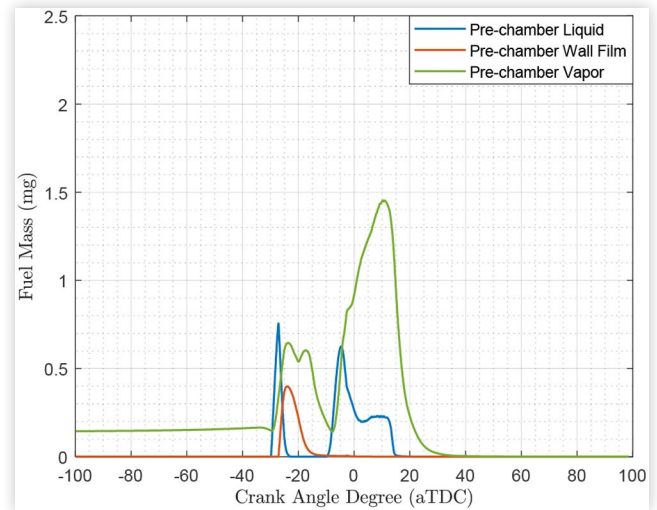
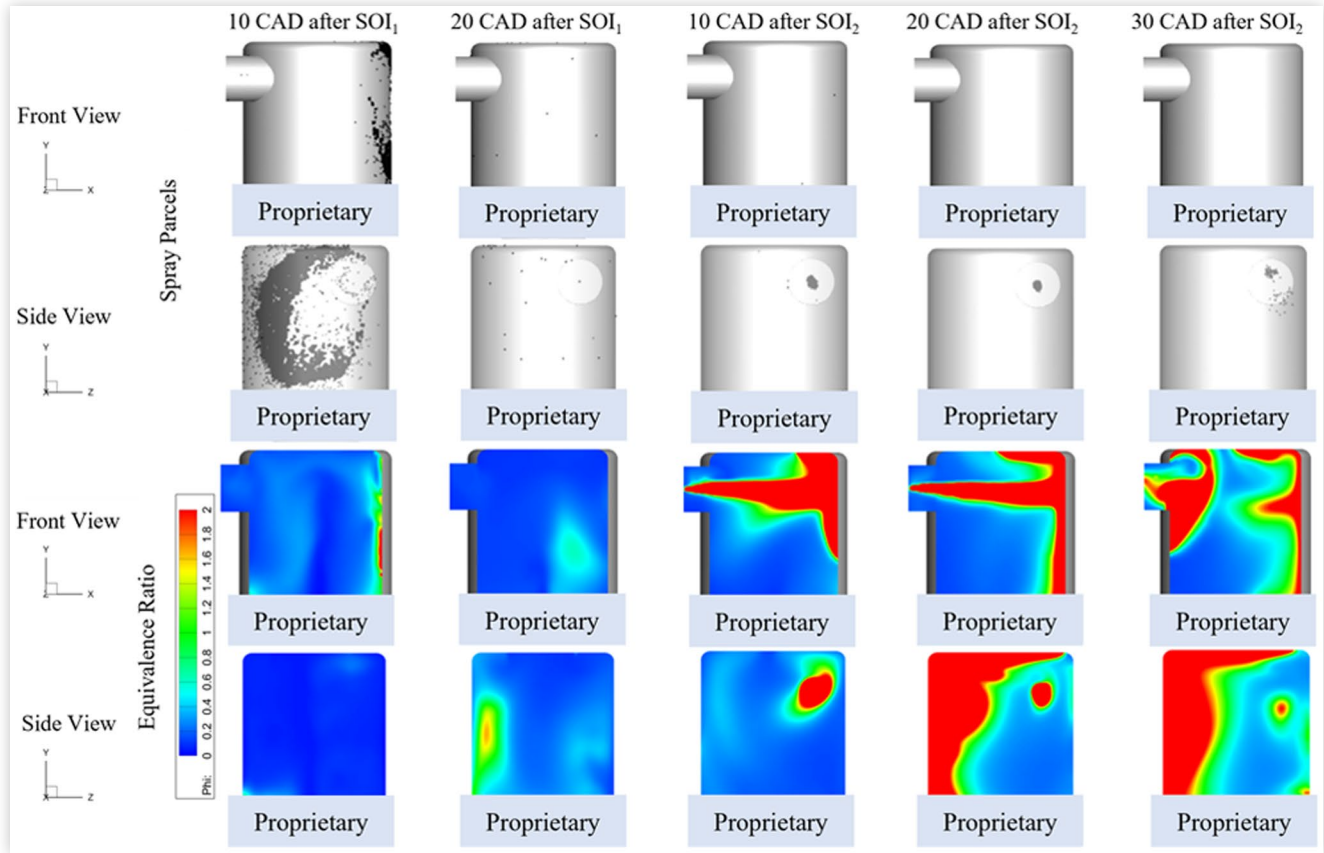


FIGURE 19 Fuel mass and state in the pre-chamber for the split-injection high-load case.



pre-chamber is shown in Figure 19 where all the liquid fuel is vaporized between -15 and -10 CAD (aTDC), which is definitely earlier than in the single injection case (Figure 16). Notably, SOI in the latter was -5 CAD (aTDC) while SOI of the main injection (8 mg) in the former was -10 CAD (aTDC). Testament to the above is provided by the combustion efficiency values in the pre-chamber of Table 5, where the metric was more than 33% higher when injection was split, while fuel was reduced solely by 10%. Additionally, the 8 nozzle holes, 85 μm wide, allow for lower droplet diameters, when compared to the 4 nozzle holes, 125 μm wide, further enhancing vaporization. Resultingly, greater mixing was achieved in the diffusion burn, as evident in the equivalence ratio visualizations between Figure 13 and Figure 20. Notably, lower peak heat release rates in split injection likely contributed to reduced heat transfer. It should be mentioned that in both high-load cases being investigated, there was essentially no fuel in the main

FIGURE 20 3D visualizations (pre-chamber) of spray parcels and equivalence ratio, in two engine views, front (top) and side (bottom) for split injection.



chamber in neither liquid state nor wall film, but the lesser amount of fuel being present as vapor could be attributed to the residuals in the main chamber at the beginning of the simulation.

Design Selection

In order to accommodate engine operation for both mid-load and high-load conditions, a universal design should be selected. In that, all engine geometry and injector geometry should result to the same compression ratio, nozzle hole count as well as nozzle hole diameter among other design specifications. With that in mind, [Table 6](#) enlists eventual engine specifications that were deemed the most beneficial to overall operation, after assessing the complete load spectrum.

The compromises considered were mostly relevant to increasing the nozzle hole count and decreasing the nozzle hole diameter at the injector. Naturally, greater injection durations would be required when injected fuel mass would almost double from the mid-load range (5 to 7 mg) to the higher load range (8 to 10 mg). All things considered, [Table 7](#) depicts the compromise between the optimal design, as assessed in the mid-load cases, and the best case with the universal design that was eventually selected.

Conclusions

The feasibility of a CI regime in a prototype rotary ICE was investigated, with the placement of integrated pre-chamber configurations to the suggested design, as proposed by LPI. The study was exclusively computational, with over 200 closed-cycle simulations conducted through CONVERGE CFD. The developed CFD models were progressively modified through iterative sensitivity analyses, between which variations to specific parameters in the respective submodels were applied. Indicatively, geometry of all pre-chamber, main chamber and injector, as well as injection strategies varied, with measured performance being monitored between each independent alteration. The latter metrics were identified in two main magnitudes: η_c and $IMEP_{g,mod}$. The application of additional limitations involved maximum injection pressure at 1000 bar as well as peak pressure in both pre-chamber and main chamber below 150 bar, whereas overall assessment involved several loading conditions. The former threshold was established due to manufacturing reasons, while the latter limit accounted for decided safety protocols.

The main findings of the study are:

1. The engine performed better at a 13.4:1 compression ratio, through resizing the overall configuration's pre-

FIGURE 21 3D visualizations (pre-chamber) of temperature and OH mass fraction, in two engine views, front (top) and side (bottom) for split injection.

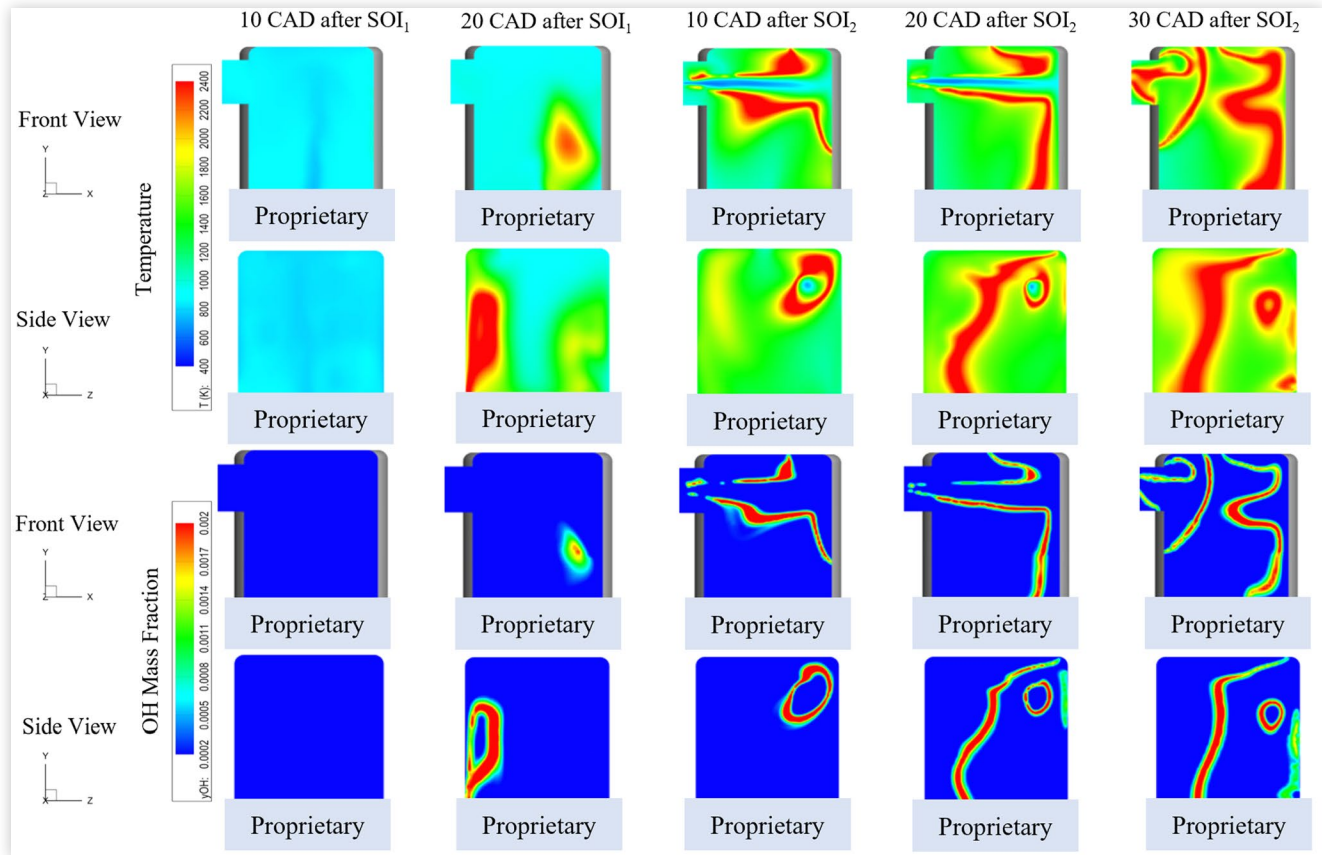


TABLE 6 Selection of the main engine and injector features.

Property	Quantity
Pre-chamber Volume	4.09 cc
Displaced Volume	69.12 cc
Compression Ratio	13.4:1
Nozzle Hole Count	8
Nozzle Diameter	85 μm

TABLE 7 Optimal-design case at mid-load conditions and best case for the universal design at the same load ($m_{\text{fuel}} = 6 \text{ mg}$).

Property	Optimal Design	Universal Design
Pre-chamber p_{peak}	142.98 bar	139.96 bar
Location (Pre-chamber)	7.11 CAD (aTDC)	7.80 CAD (aTDC)
Main Chamber p_{peak}	147.60 bar	142.83 bar
Location (Main Chamber)	2.61 CAD (aTDC)	3.10 CAD (aTDC)
HRR _{peak}	22.84 J/CAD	18.78 J/CAD
Location	-6.29 CAD (aTDC)	-6.10 CAD (aTDC)
Pre-chamber η_c	81.27%	81.30%
Total η_c	98.00%	97.47%
IMEP _{g,mod}	17.62 bar	15.81 bar

chamber. Examination of both lower and higher compression ratios, ranging from 7% lower to 20% higher, resulted to worse-performing systems. This is believed to be due to the change in pre-chamber size when altering the compression ratio, which drastically affected combustion in the pre-chamber. If a higher compression ratio is desired, a different overall design will be required.

- Nozzle hole count and diameter of the injector, along with injection duration were the main factors in limiting peak injection pressure.
- The selection of 4 nozzle holes seemingly resulted in better engine performance in mid-load cases (6 mg of diesel), with results outperforming the choice of 2, 6 and 8 holes, mainly due to the greater heat release. Droplet diameter was small enough to allow for enhanced vaporization but large enough to result in effective transitioning to the diffusion-burn phase.
- Greater nozzle diameters did not translate to improved performance, apart from the cases accounting for late combustion phasing, in which SOI was phased later than 5 CAD (bTDC). Lower vaporization rates due to lower surface-to-volume ratios along with additional compression work and heat transfer due to increased peak pressures and

temperatures seemed to deter overall performance by shifting operation to the region of diminishing returns.

5. Better engine scavenging and higher altitude conditions culminated to the engine performing its best at 98% (η_c), in the mid-load cases. Specifically, larger air mass quantities were trapped in the cylinder; thus, shifting operation to leaner regions, while effective pressure gains were raised despite heightened peak cylinder pressure (147.60 bar) and consequent heat transfer losses.
6. The single-injection strategy did not translate to better performance for the high-load case. The lower AFR along with the prolonged wall wetting of the pre-chamber during core combustion resulted in lower combustion efficiency when compared to the mid-load cases.
7. Split-injection strategy along with increasing the trapped air mass increased both combustion efficiency and IMEP_{g,mod}. The latter was raised from 80.75% for the single-injection high-load case to 86.18%, with gross effective pressure gains being raised by almost 5%. Essentially, enhanced fuel vaporization due to greater temperatures resulting from the combustion of the pilot injection, as well as shorter ignition delays due to lower nozzle hole diameters that allowed for greater mixing, favored the particular strategy over single injection. Indicatively, effective pressure gains were increased while fuel consumption was decreased by 10% from the single-injection high-load case.
8. The universal design established for both mid-load and high-load cases resulted in compromising the engine's performance in the former. While η_c was approximated marginally lower at 97.47%, IMEP_{g,mod} dropped by more than 10%. Doubling the nozzle hole count and reducing nozzle hole diameter by 32%, led to significantly lower effective pressure gains and roughly the same levels of efficiency in combustion.

References

1. Fyffe, J.R., Donohue, M.A., Regalbuto, M.C., and Edwards, C.F., "Mixed Combustion-Electrochemical Energy Conversion for High-Efficiency, Transportation-Scale Engines," *International Journal of Engine Research* 18, no. 7 (2017): 701-716, doi:<https://doi.org/10.1177/1468087416665936>.
2. Abas, N., Kalair, A., Khan, N., and Kalair, A.R., "Review of GHG Emissions in Pakistan Compared to SAARC Countries," *Renewable and Sustainable Energy Reviews* 80 (2017): 990-1016, doi:<https://doi.org/https://doi.org/10.1016/j.rser.2017.04.022>.
3. Blank, D.A., "Methane/CNG Combustion in a DI Radical-Ignition Rotary Engine with Low-Heat Rejection," SAE Technical Paper 2007-01-1912, 2007, doi:<https://doi.org/10.4271/2007-01-1912>.
4. Keros, P.E., Assanis, D., Schlechtweg, J., and Wooldridge, M.S., "Fast Methods to Analyze High-Speed Images of HCCI and Spark-Assisted HCCI Ignition Events," in *Presented at the ASME 2010 Internal Combustion Engine Division Fall Technical Conference*, 2010.
5. Zigler, B.T., Keros, P.E., Helleberg, K.B., Fatouraie, M. et al., "An Experimental Investigation of the Sensitivity of the Ignition and Combustion Properties of a Single-Cylinder Research Engine to Spark-Assisted HCCI," *International Journal of Engine Research* 12, no. 4 (2011): 353-375, doi:<https://doi.org/10.1177/1468087411401286>.
6. Hariharan, D., Gainey, B., Yan, Z., Mamalis, S. et al., "Experimental Study of the Effect of Start of Injection and Blend Ratio on Single Fuel Reformate RCCI," *Journal of Engineering for Gas Turbines and Power* 142, no. 8 (2020): 081010, doi:<https://doi.org/10.1115/1.4047814>.
7. Bunce, M., Blaxill, H., Kulatilaka, W., and Jiang, N., "The Effects of Turbulent Jet Characteristics on Engine Performance Using a Pre-Chamber Combustor," SAE Technical Paper 2014-01-1195, 2014, doi:<https://doi.org/10.4271/2014-01-1195>.
8. Kulatilaka, W., Jiang, N., Bunce, M., and Blaxill, H., "The Effects of Turbulent Jet Characteristics on Engine Performance Using a Pre-Chamber Combustor," SAE Technical Paper 2014-01-1195, 2014, doi:<https://doi.org/10.4271/2014-01-1195>.
9. Assanis, D., Engineer, N., Neuman, P., and Wooldridge, M., "Computational Development of a Dual Pre-Chamber Engine Concept for Lean Burn Combustion," SAE Technical Paper 2016-01-2242, 2016, doi:<https://doi.org/10.4271/2016-01-2242>.
10. Mattarelli, E., Cantore, G., Rinaldini, C.A., and Savioli, T., "Combustion System Development of an Opposed Piston 2-Stroke Diesel Engine," *Energy Procedia* 126 (2017): 1003-1010, doi:<https://doi.org/https://doi.org/10.1016/j.egypro.2017.08.268>.
11. Phillips, F., Gilbert, I., Pirault, J., and Megel, M., "Scuderi Split Cycle Research Engine: Overview, Architecture and Operation," *SAE Int. J. Engines* 4, no. 1 (2011): 450-466, doi:<https://doi.org/https://doi.org/10.4271/2011-01-0403>.
12. Yuen, W.W., Andon, J., and Bajulaz, R., "The Bajulaz Cycle: A Two-Chamber Internal Combustion Engine with Increased Thermal Efficiency," SAE Technical Paper 860534, 1986, doi:<https://doi.org/10.4271/860534>.
13. Thompson, G.J., Wowczuk, Z.S., and Smith, J.E., "Rotary Engines—A Concept Review," SAE Technical Paper 2003-01-3206, 2003, doi:<https://doi.org/10.4271/2003-01-3206>.
14. Britt, R., "Variable Explosion-Displacement Rotary Engine," Google Patents, 1973.
15. Takahashi, M., "Constant Pressure Heating Vane Rotary Engine," Google Patents, 1976.
16. Norbye, J.P., *The Wankel Engine: Design, Development Applications*, (Chilton Book Company, 1971).
17. Turner, J., Turner, M., Islam, R., Shen, X. et al., "Further Investigations into the Benefits and Challenges of Eliminating Port Overlap in Wankel Rotary Engines," SAE Technical Paper 2021-01-0638, 2021, doi:<https://doi.org/10.4271/2021-01-0638>.

18. Shkolnik, N. and Shkolnik, A., "Rotary High Efficiency Hybrid Cycle Engine," SAE Technical Paper [2008-01-2448](https://doi.org/10.4271/2008-01-2448), 2008, doi:<https://doi.org/10.4271/2008-01-2448>.
19. Eiermann, D., Nuber, R., and Soimar, M., "The Introduction of a New Ultra-Lite Multipurpose Wankel Engine," SAE Technical Paper [900035](https://doi.org/10.4271/900035), 1990, doi:<https://doi.org/10.4271/900035>.
20. Savvakis, S., Gkoutzamanis, V., and Samaras, Z., "Description of a Novel Concentric Rotary Engine," SAE Technical Paper [2018-01-0365](https://doi.org/10.4271/2018-01-0365), 2018, doi:<https://doi.org/10.4271/2018-01-0365>.
21. Pehan, S. and Kegl, B., "Rotary Engine Design," SAE Technical Paper [2001-01-3194](https://doi.org/10.4271/2001-01-3194), 2001, doi:<https://doi.org/10.4271/2001-01-3194>.
22. Leboeuf, M., Dufault, J., Nickerson, M., Becker, K. et al., "Performance of a Low-Blowby Sealing System for a high Efficiency Rotary Engine," SAE Technical Paper [2018-01-0372](https://doi.org/10.4271/2018-01-0372), 2018, doi:<https://doi.org/10.4271/2018-01-0372>.
23. Shapovalov, V., "The Two-Stroke Rotary Diesel Engine," SAE Technical Paper [1999-01-2888](https://doi.org/10.4271/1999-01-2888), 1999, doi:<https://doi.org/10.4271/1999-01-2888>.
24. Karatsu, Y., Minota, S., Hashimoto, H., Moriue, O. et al., "Simultaneous Observation of Combustion in Optical Rotary Engine by Bottom View and Side View," SAE Technical Paper [2015-01-1891](https://doi.org/10.4271/2015-01-1891), 2015, doi:<https://doi.org/10.4271/2015-01-1891>.
25. Badr, O., Naik, S., O'Callaghan, P.W., and Probert, S.D., "Rotary Wankel Engines as Expansion Devices in Steam Rankine-Cycle Engines," *Applied Energy* 39, no. 1 (1991): 59-76, doi:[https://doi.org/https://doi.org/10.1016/0306-2619\(91\)90063-4](https://doi.org/https://doi.org/10.1016/0306-2619(91)90063-4).
26. Kweon, C.B.M., *A Review of Heavy-Fueled Rotary Engine Combustion Technologies*, (Army Research Lab Aberdeen Proving Ground MD, 2011).
27. Louthan, L., "Development of a Lightweight Heavy Fuel Rotary Engine," SAE Technical Paper [930682](https://doi.org/10.4271/930682), 1993, doi:<https://doi.org/10.4271/930682>.
28. Richards, K.J., Senecal, P.K., and Pomraning, E., *Converge 3.0*, (Madison, WI: Convergent Science, 2021).
29. Wang, F., Reitz, R., Pera, C., Wang, Z. et al., "Application of Generalized RNG Turbulence Model to Flow in Motored Single-Cylinder PFI Engine," *Engineering Applications of Computational Fluid Mechanics* 7 (2013): 486-495, doi:<https://doi.org/10.1080/19942060.2013.11015487>.
30. Schmidt, D.P. and Rutland, C.J., "A New Droplet Collision Algorithm," *Journal of Computational Physics* 164, no. 1 (2000): 62-80, doi:<https://doi.org/https://doi.org/10.1006/jcph.2000.6568>.
31. Amsden, A.A., O'Rourke, P.J., and Butler, T.D., "Kiva-2: A Computer Program for Chemically Reactive Flows with Sprays," United States, 1989, <https://doi.org/10.2172/6228444>.
32. O'Rourke, P.J. and Amsden, A.A., "A Spray/Wall Interaction Submodel for the Kiva-3 Wall Film Model," SAE Technical Paper [2000-01-0271](https://doi.org/10.4271/2000-01-0271), 2000, doi:<https://doi.org/10.4271/2000-01-0271>.
33. Senecal, P.K., Pomraning, E., Richards, K.J., Briggs, T.E. et al., "Multi-Dimensional Modeling of Direct-Injection Diesel Spray Liquid Length and Flame Lift-Off Length Using CFD and Parallel Detailed Chemistry," SAE Technical Paper [2003-01-1043](https://doi.org/10.4271/2003-01-1043), 2003, doi:<https://doi.org/10.4271/2003-01-1043>.
34. Nordin, N., "Numerical Simulations of Non-Steady Spray Combustion Using a Detailed Chemistry Approach," Licentiate of Engineering thesis, Department of Thermo and Fluid Dynamics, Chalmers University of Technology, Goteborg, Sweden, 1998.
35. John, B.H., *Internal Combustion Engine Fundamentals*, (McGraw-Hill Education, 2018).

Contact Information

Prof. Dimitris Assanis (dimitris.assanis@stonybrook.edu)

Assistant Professor
Dept. of Mechanical Engineering
Stony Brook University
116 Light Engineering
100 Nicholls Rd
Stony Brook, NY 11794
USA

Dr. Alec Shkolnik (ashkolnik@liquidpiston.com)

President & CEO
LiquidPiston, Inc.
1292a Blue Hills Avenue
Bloomfield, CT 06002
USA

Acknowledgments

This material is based upon work supported by the United States Air Force AFRL/SBRK under Contract No. FA8649-21-P-0048. The authors would like to also thank Stony Brook Research Computing and Cyberinfrastructure, and the Institute for Advanced Computational Science at Stony Brook University for access to the SeaWulf computing system, which was made possible by a \$1.4M National Science Foundation grant (#1531492).

Definitions/Abbreviations

AFR - air-to-fuel ratio
AMR - adaptive mesh refinement
APU - auxiliary power unit
aTDC - after top dead center
BDC - bottom dead center
bTDC - before top dead center
CAD - crank angle degrees
CCI - conditional compression ignition
CFD - computational fluid dynamics
CI - compression ignition
CR - compression ratio
DOE - design of experiments
GHG - greenhouse gas

HCCI - homogeneous charge compression ignition

HRR_{peak} - peak heat release rate

IACS - Institute for Advanced Computational Science

ICE - internal combustion engine

IMEP - indicated mean effective pressure

IMEP_{g,mod} - indicated mean effective pressure criterion

LPI - LiquidPiston Inc.

NTC - no-time-counter

p_{peak} - peak pressure

RANS - Reynolds-averaged Navier-Stokes

RCCI - reactivity controlled compression ignition

RNG - re-normalization group

SI - spark ignition

SOI - start of injection

TDC - top dead center

UAV - unmanned air vehicle

UHC - unburned hydrocarbons

VS - Vladimir Shapovalov

η_c - combustion efficiency

φ - equivalence ratio